IOP Publishing Physica Scripta
Phys. Scr. 95 (2020) 045802 (13pp) https://doi.org/10.1088/1402-4896/ab5e45

Octahedral distortion and correlated electrical conduction of corundum type $Co_4Ta_2O_9$ and $Co_4Nb_2O_9$

Parthasarathi Mohanty and Sunita Keshri

Department of Physics, Birla Institute of Technology, Mesra, Ranchi, 835215, India

E-mail: parthacartoon@gmail.com and mohantyparthasarathi05@gmail.com

Received 9 August 2019, revised 24 November 2019
Accepted for publication 3 December 2019
Published 12 February 2020

Abstract

The structural, elemental and electrical conductivity properties along with the relaxor phenomena are studied for corundum type $Co_4Ta_2O_9$ and $Co_4Nb_2O_9$ ceramics. The refined x-ray diffraction results confirm that the unit cells of both the ceramics are isostructural to $Mg_4Ta_2O_9$. A comparative study of polyhedral distortion shows that $(Ta/Nb)O_6$ octahedra are more distorted than CoO_6 octahedra. X-ray photoelectron spectra of $Co_4Ta_2O_9$ and $Co_4Nb_2O_9$ compositions reveal that the majority of Co ions possess high spin 2+ oxidation state, whereas both Ta and Nb ions exhibit reduction in their oxidation state to 4+ suboxide state on the surface, because of the generation of oxygen vacancies along with trapped electrons in $(Ta/Nb)_2O_9$ species. The effects of defect chemistry, ionic vacancies and crystal distortion on the charge transport and relaxor phenomenon are analyzed using impedance measurement over a wide range of temperature (30 °C–275 °C) and frequency (100 Hz–1 MHz). The frequency exponent η versus T plot of $Co_4Ta_2O_9$ proposes that both correlated barriers hopping and small polaron tunneling are the principal charge transport mechanisms at high and low-temperature regimes respectively. In this composition, at high-temperature regime vacancy trapped electrons are the major charge carriers, whereas at low-temperature regime the charge carriers are small polarons. For $Co_4Nb_2O_9$, a single conduction process is observed above 5 kHz frequency where overlapping large polarons tunneling is the predominant conduction mechanism and below this frequency, electrode polarization prevails.

Keywords: polyhedral distortion, XPS, charge transport, conduction model, relaxation process

(Some figures may appear in colour only in the online journal)

1. Introduction

In the last few decades, corundum type $A_4B_2O_9$ (A = Mg, Co, Mn, B = Ta, Nb) ceramics have attracted much attention as promising materials for the manufacturing of microwave dielectric devices due to their large quality factor, low loss (tan δ) and reasonable dielectric constant (ε_r) [1, 2]. Apart from their microwave dielectric properties, spin flop phase transition and magnetoelectric (ME) response of $Co_4Ta_2O_9$ and $Co_4Nb_2O_9$ compositions have motivated many researchers to innovate various next-generation multifunctional electronic devices [3–6]. Both these compositions were first synthesized by Bertaut *et al* [7] in 1961 and their ME effect was discovered by Fischer *et al* [8] in 1972. Interest in these compositions has grown suddenly by few recent publications [3–5], where ME effect and polarization properties have been discussed extensively. Fang *et al* [4, 5] have noticed that the dielectric anomaly and electric polarization induced by the applied magnetic field in $Co_4Ta_2O_9$ and $Co_4Nb_2O_9$ are the consequences of spin fluctuation and domain effect. An experimental and theoretical combined study has been carried out by Solovyev and Kolodiazhnyi [3] on both the compositions and they have revealed that $Co_4Ta_2O_9$ is magnetically softer than $Co_4Nb_2O_9$, because of the easier deformation in structure and larger production of polarization in presence of the external magnetic field. The crystal structures of these ceramics are isostructural to $Mg_4Ta_2O_9$, which

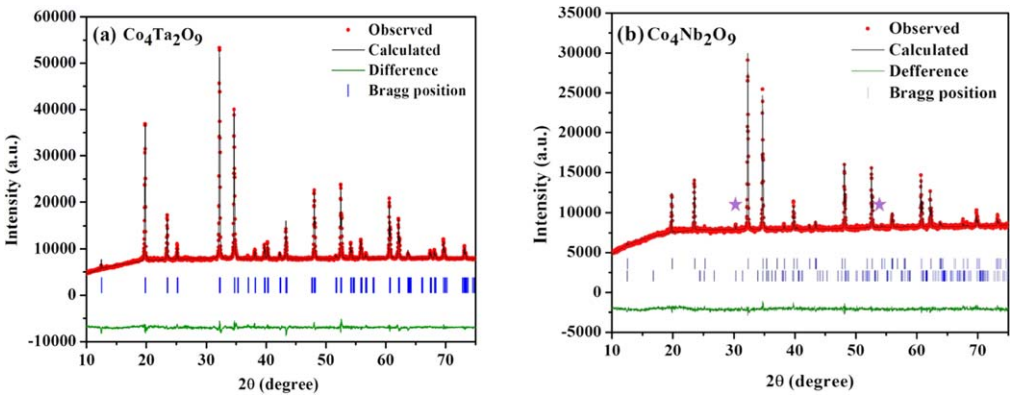

Figure 1. Rietveld analysis results of room temperature XRD patterns for (a) $Co_4Ta_2O_9$ and (b) $Co_4Nb_2O_9$ ceramics. Asterisked (★) peak correspond to the second phase, $CoNb_2O_6$.

is a modified corundum ($\alpha - Al_2O_3$) structure [9]. The crystal consists of alternating honeycomb layers associated with hexagonal rings of CoO_6 octahedra [6]. Octahedrons present in the unit cell, form Co_2O_9 and $(Ta/Nb)_2O_9$ types groups by sharing their face. These groups exhibit polyhedral distortion which is an outcome of cation-cation repulsion [10]. Castellanos *et al* [11] have reported that the NbO_6 octahedrons are more distorted than CoO_6 octahedrons in $Co_4Nb_2O_9$ ceramics.

However, in all these above studies, few major aspects like, polyhedral distortion, defect chemistry, and elemental oxidation states have not been investigated thoroughly. The possibility of valence state fluctuations in transition elements like Co, Nb, and Ta may often influence the defect chemistry and crystal order. Therefore, it is important to identify their charge states to analyze the crystal behavior and its possible defects. The crystal defects determine the possible charge carriers which play a significant role in the transport process. The analysis of conduction property and defect chemistry along with crystal distortion above room temperature has not been reported yet. In our previous work [12], we have reported about the consequences of structural distortion on charge transport, crystal defects and relaxor response for Co_3O_4 added corundum type $Mg_4Ta_2O_9$ ceramics. It has been observed that A-site substitution takes place up to 30% Co addition and beyond that, B-site substitution takes place in order to maintain charge neutrality in crystal. This study was carried out for partial substitution of Mg by Co ions in $Mg_4Ta_2O_9$. For 100% substitution of Co (eliminating Mg totally by Co addition) on A-site is yet to be analyzed.

Therefore, in this paper, an analytical study has been carried out above room temperature (up to 275 °C) for $Co_4Ta_2O_9$ and $Co_4Nb_2O_9$ ceramics to investigate the structural, elemental and conduction properties along with the relaxor response.

2. Experimental

Polycrystalline $Co_4Ta_2O_9$ and $Co_4Nb_2O_9$ ceramics were prepared using the solid-state reaction method. High purity Co_3O_4 (Sigma-Aldrich, 99.5%) powder was mixed with Ta_2O_5 (Sigma-Aldrich, 99.99%) and Nb_2O_5 (Sigma-Aldrich, 99.99%) powder stoichiometrically (with the nominal ratio 4:2:9) to synthesize $Co_4Ta_2O_9$ and $Co_4Nb_2O_9$ ceramics respectively. The mixed powder was ground in an agate mortar for 6 h and then calcined for 10 h in a muffle furnace at 900 °C. The calcined powder was pressed into cylindrical pellets of 10 mm diameter and ~2 mm thickness with the help of hydraulic press at 150 Kg cm^{-2}. Then the pellets were sintered at 1100 °C for 5 h at a heating rate of 5 °C min^{-1} in the air as reported previously [4, 13].

The phase purity and crystallinity were identified by x-ray diffraction using Cu K_α ($\lambda = 0.154\,06$ nm) irradiation at room temperature. Rietveld analysis technique was used to investigate lattice parameters and crystal structure. The structural stability and phase transition were checked by high-temperature x-ray diffraction in a temperature range from 50 °C to 275 °C. The microstructure study was carried out using JEOL-6330F scanning electron microscope. The chemical states of various elements present in both ceramics were investigated by PHI 5000 Versa Prob-II, FEI Inc., x-ray photoelectron spectroscopy (XPS) using monochromatic Al K_α irradiation. High-resolution scanning of core levels was carried out for one hour to each element with pass energy 23.5 eV and step size 0.025 eV per 50 ms acquisition time to obtain high-quality photoelectron spectra. Finally, to characterize the bulk conductivity properties, the sintered pellets of different compositions were painted each side with high purity conducting silver paste and were dried at 200 °C for 1 h to remove moisture before taking any electrical measurement. A Solatron, gain-phase analyzer (model-1260) was used to measure dielectric properties, like dielectric loss ($\tan\delta$), capacitance (C_p) and complex impedance (Z^*) in the radio frequency range of 100 Hz–1 MHz and the temperature range of 30 °C–275 °C in an interval of 25 °C.

3. Results and discussion

3.1. X-ray diffraction analysis

The Rietveld refinement of x-ray diffraction patterns obtained using FullProf 2000 software for $Co_4Ta_2O_9$ and $Co_4Nb_2O_9$ ceramics, sintered at 1100 °C for 5 h, is shown in figures 1(a) and (b) respectively. The refined results yield an excellent

Table 1. Structure parameters and reliability indicators obtained from Rietveld refinement of x-ray diffraction data at room temperature.

Composition	Atom	Site	Fractional coordinates			B_{iso} (Å^2)	Lattice parameters	Statistical parameters
			x	y	z			
$Co_4Ta_2O_9$	Co1	4d	0.3333	0.6667	0.0101	0.2187	$a = b$ (Å) = 5.1706	R_p(%) = 10.57
	Co2	4d	0.3333	0.6667	0.3157	0.2771	c (Å) = 14.1445	R_{wp}(%) = 13.00
	Ta	4c	0.0000	0.0000	0.3573	0.1539	V(Å^3) = 327.4929	R_{exp}(%) = 8.34
	O1	12g	0.3167	0.2789	0.0815	0.0276	χ^2 (%) = 2.42	R_{Bragg} (%) = 7.84
	O2	6f	0.3132	0.0000	0.2500	1.0059		
$Co_4Nb_2O_9$	Co1	4d	0.3333	0.6667	0.0153	0.0789	$a = b$ (Å) = 5.1613	R_p(%) = 13.34
	Co2	4d	0.3333	0.6667	0.3157	0.1050	c (Å) = 14.1066	R_{wp}(%) = 17.20
	Nb	4c	0.0000	0.0000	0.3608	0.0529	V(Å^3) = 326.4490	R_{exp}(%) = 10.80
	O1	12g	0.3260	0.2980	0.0790	0.0268	χ^2 (%) = 2.54	R_{Bragg} (%) = 13.17
	O2	6f	0.3112	0.0000	0.2500	0.3418		

agreement between the observed (I_{obs}) and calculated (I_{cal}) diffraction profiles with no peak left unindexed. Figure 1(a) shows the formation of single-phase $Co_4Ta_2O_9$ polycrystalline compound, whereas in figure 1(b), an additional second phase of $CoNb_2O_6$ with a small weight percentage (~5%) appears along with its major phase $Co_4Nb_2O_9$. The appearance of secondary phase may be the outcome of the incomplete reaction of starting precursors or high-temperature decomposition of the target phase. A similar argument has been put forward by Kolodiazhnyi *et al* [14] to explain the formation of secondary phase along with the primary phase of $Ba_3M'M''_2O_9$. The refinement analysis of $Co_4Ta_2O_9$ and $Co_4Nb_2O_9$ confirms that the unit cells are of corundum type ($\alpha - Al_2O_3$) centro-symmetric, having crystal structure trigonal and space group $P\bar{3}c1$ (no. 165). The minor phase, $CoNb_2O_6$, which coexists along with major phase, $Co_4Nb_2O_9$ belongs to the orthorhombic *Pbcn* space group (no. 60). The refined lattice parameters of the minor phase $CoNb_2O_6$ are $a = 14.1785$ Å, $b = 5.6994$ Å, and $c = 5.0367$ Å. Two formula units built up by three unit cells can be assigned to the unit cell of $Co_4M_2O_9$ (M = Ta and Nb). The Co and Ta/Nb—ions occupy the Al-site with the ratio 2:1. The obtained atomic coordinates, lattice parameters, the volume of the unit cell, reliability factors (*R*-factors like R_p, R_{wp}, R_{exp}, and R_{Bragg}) and goodness of fit values (χ^2) are reported in table 1. It can be noticed that in between $Co_4Ta_2O_9$ and $Co_4Nb_2O_9$ ceramics, there are not much differences in their lattice parameters and unit cell volume, because of the similar ionic radii and same oxidation states of Ta and Nb ions. During the refinement process, it was observed that low χ^2 value can be achieved by assigning two crystallographic inequivalent symmetry positions to the oxygen (O(1) and O(2)) and cobalt (Co(1) and Co(2)) ions. A schematic diagram of $Co_4M_2O_9$ (M = Ta and Nb) ceramics obtained from the refined structure is illustrated in figure 2(a), where two layers of CoO_6 octahedra are sandwiched between two $(Ta/Nb)O_6$ octahedral layers. In these octahedra, the central atoms are occupied by the cations (Co and Ta/Nb ions) and the corners are occupied by anions (oxygen ions). The inter-ionic distances between the central cation and its corner anions are presented in table 2. It can be noticed that the inter-ionic distances of Co(1)–O in a $Co(1)O_6$ octahedron is very close to one another, showing less polyhedral distortion. In the case of $(Ta/Nb)O_6$ octahedron, the distance of Ta/Nb–O(2) is much larger than Ta/Nb–O(1). As a result of this large difference, $(Ta/Nb)O_6$ octahedron shows a large degree of polyhedral distortion. The inter-ionic oxygen-oxygen distances of a triangular face, which is shared by two conjugate octahedrons, are found to be smaller than the other face. Tarakina *et al* [10] have reported that the central cations present in face shared octahedrons always repel each other in corundum structured ceramics like; $Mg_4Ta_2O_9$, $Mn_4Nb_2O_9$, and $Zn_4Nb_2O_9$, which results octahedrons with distorted geometry. The relative degree of distortion (σ) can be calculated [10] by

$$\sigma = \sqrt{\sum_{i=1}^{N} \left| 1 - \frac{R_i}{\sum_{i=1}^{N} R_i / N} \right|^2}, \qquad (1)$$

where N and R_i are the coordination number and metal-oxygen distance respectively. The calculated relative degrees of distortions for various octahedra are presented in table 3. It can be noticed that CoO_6 octahedrons of $Co_4Ta_2O_9$ and $Co_4Nb_2O_9$ ceramics show fewer degrees of polyhedral distortion than our reported [12] MgO_6 octahedral distortion values, obtained for $Mg_4Ta_2O_9$ ceramic ($\sigma = 0.277$ and 0.132 for $Mg(1)O_6$ and $Mg(2)O_6$ octahedrons respectively). On the contrary, the $(Ta/Nb)O_6$ octahedrons of both the compositions show larger σ value (= 0.273 and 0.251 respectively for TaO_6 and NbO_6 octahedrons) than TaO_6 octahedrons of $Mg_4Ta_2O_9$ (= 0.151) suggesting more distortion in the Ta/Nb polyhedra.

The x-ray diffraction results confirm that in $Co_4Ta_2O_9$ and $Co_4Nb_2O_9$ ceramics, each octahedron is more or less distorted in its structures. This distortion is due to the cationic repulsion generated between the face shared octahedrons; mainly Ta/Nb–Ta/Nb and Co(1)–Co(2) repulsion in $(Ta/Nb)_2O_9$ and Co_2O_9 groups respectively. As a result, slight shifting in atomic coordinates is observed along the z-direction. It reciprocates on both sides of the inversion center. The refinement results presented in table 1 exhibits that out of the fractional atomic coordinates, the x and y remain unchanged for Co and Ta/Nb ions, whereas only the z value alters. Castellanos *et al*

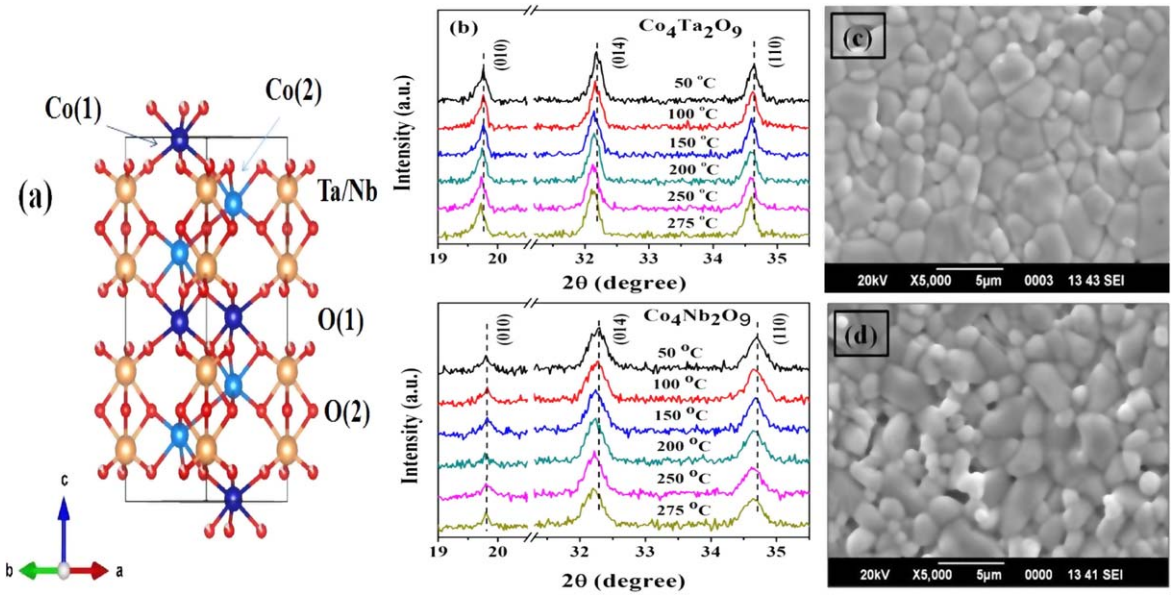

Figure 2. (a) Crystal structure of $Co_4(Ta/Nb)_2O_9$; (b) high temperature x-ray diffraction spectra of $Co_4Ta_2O_9$ and $Co_4Nb_2O_9$ (three reflections are shown for legibility); SEM images of (c) $Co_4Ta_2O_9$ and (d) $Co_4Nb_2O_9$ ceramics.

[11] have also observed identical distortion in CoO_6 and NbO_6 polyhedra for $Co_4Nb_2O_9$ ceramics.

In order to analyze the structural phase transition of $Co_4Ta_2O_9$ and $Co_4Nb_2O_9$ ceramics, temperature-dependent x-ray diffraction has been carried out for the temperature range of 50 °C–275 °C at a regular interval of 50 °C. The diffraction spectra obtained at various temperatures have been presented in figure 2(b), where three reflections are shown for legibility. It was observed that with the rise in temperature the peaks shift towards lower 2θ without the appearance of any additional peak or any anomalous behavior. This shifting is generated due to the thermal expansion of lattice parameters. Within the temperature range of our interest, no structural phase transition has been observed. However, there may be a possibility of a magnetic phase transition in this temperature range, which is beyond the scope of our present study.

The microstructure images of $Co_4Ta_2O_9$ and $Co_4Nb_2O_9$ ceramics, sintered at 1100 °C are presented in figures 2(c) and (d) respectively. In both figures, it can be noticed that the grains are well defined. The average grain size is about 2–3 μm.

3.2. X-ray photo-electron spectra study

The XPS analysis was performed to obtain information about surface chemistry and the oxidation states of various elements present in $Co_4Ta_2O_9$ and $Co_4Nb_2O_9$ ceramics. The photo-electron spectra of core level electrons are useful to analyze the chemical bonding present in complex compounds. In such compounds, when metal interacts with oxygen, rearrangement of electronic levels takes place in both cation and anion by the transfer of valence electron from the metal atom to oxygen. This displacement of valence electron away from the metal nucleus reduces the screening effect in between the core level electrons; resulting in an increase in their binding energy. This screening effect can be noticed by observing the variation of their photo-peak position [15, 16]. Therefore, the XPS characterization was carried out to obtain the core level photo-electron spectra of Co 2p, Ta 4f, Nb 3d and O 1s of $Co_4Ta_2O_9$ and $Co_4Nb_2O_9$ ceramics. The obtained spectra are presented in figures 3(a)–(f).

However, our purpose is to identify the oxidation state of cobalt ions present in $Co_4Ta_2O_9$ ceramic by taking the main line and satellite peaks into consideration. In figure 3(a) the XPS spectrum of Co shows two components ($2p_{3/2}$ and $2p_{1/2}$), originated due to the spin-orbital splitting. Each component exhibits a main line (at 780.06 eV for $2p_{3/2}$ component and 796.16 eV for $2p_{1/2}$ component) along with a satellite peak (appeared at 785.7 and 802.2 eV), situated above the main line. Literature survey [17–22] reveals that binding energy of $2p_{3/2}$ of Co^{2+} and Co^{3+} for octahedral oxygen environment is relatively close, therefore the oxidation state of Co must be determined by their satellite peaks, generally appear 3.6–6.5 eV above the main $2p_{3/2}$ line. High spin Co^{2+} core level spectrum (as in CoO) shows strong satellite peak above the main 2p line, whereas low spin Co^{2+} compounds either exhibit weak or missing satellites in their photoelectron spectrum [19]. Similarly, Co^{3+} with octahedral geometry shows strongly suppressed satellite peak due to the reduction of charge transfer in the shakeup processes [20]. In our case (in figure 3(a)), the satellite peaks appeared at ~6 eV above the main line are intense and distinguishable. Therefore, it can be argued that Co may possess high spin 2+ oxidation states. The intensity and the energy position of satellite peaks in photoelectron spectra of 3d transition metal oxides strongly depend upon three factors; cation valency, ionic environment and electron occupancy [22]. The core holes, which are created during the photoelectron emission in 2p core-level, influence strongly the energy positions of the ionic orbital. It leads to a pair of charge compensation processes. One of these corresponds to the charge transfer from ligand to the 3d orbital which effectively

Table 2. Selected inter ionic distances (Å) for $Co_4Ta_2O_9$ and $Co_4Nb_2O_9$ ceramics.

Composition	Co(1) −O(1)[i]	Co(1) −O(1)[ii]	Co(2) −O(1)	Co(2) −O(2)	(Ta/Nb) –O(1)	(Ta/Nb)–O(2)	Co(1) –(Ta/Nb)	Co(2) −(Ta/Nb)	(Ta/Nb) −(Ta/Nb)
$Co_4Ta_2O_9$	2.1269 × 3	2.2076 × 3	2.2263 × 3	2.0058 × 3	1.7742 × 3	2.2207 × 3	3.5248	3.0427	3.0374
$Co_4Nb_2O_9$	2.1386 × 3	2.0874 × 3	2.2384 × 3	2.0071 × 3	1.8248 × 3	2.2412 × 3	3.4546	3.0470	3.1260

Note. (i) and (ii) are the two symmetry positions.

Table 3. The relative degree of distortion for different octahedra of $Co_4Ta_2O_9$ and $Co_4Nb_2O_9$ ceramics.

Composition	$Co(1)O_6$	$Co(2)O_6$	$(Ta/Nb)O_6$
$Co_4Ta_2O_9$	0.045	0.127	0.273
$Co_4Nb_2O_9$	0.029	0.133	0.251

screens the core hole and is associated with the mainline. This screened state can be represented by $|2p^53d^{n+1}\underline{L}\rangle$, where $\underline{L}$ represents the ligand hole and n represents the number of valence electrons. The other one corresponds to the unscreened states of higher energy where the charge compensation is provided by *sp* orbitals. This sate can be represented by $|2p^53d^n\rangle$. Out of these two final sates, the lowest energy is associated with the main 2p line while the higher energy is associated with the satellite lines. This effect is known as ligand-to-metal charge transfer or shake-up. Therefore, both the ligand environment and the oxidation state of metal have major role in charge transfer process.

For further analysis, the main lines were deconvoluted corresponding to different states of Cobalt, using parameter controlled Gaussian-Lorentzian peaks, after proper background correction. The deconvoluted spectra reveal that the main lines (both $2p_{3/2}$ and $2p_{1/2}$) are best fitted with two spectra each corresponding to Co^{2+} and Co^{3+} ions, whereas their relative satellites are fitted with single spectrum. The binding energies of the deconvoluted spectra present in the $2p_{3/2}$ photo-peak are 779.71 and 780.90 eV respectively for Co^{3+} and Co^{2+} ions. The Co^{2+}: Co^{3+} area ratio obtained from the fitting is 2.5 which suggests that the major species is mainly divalent Co ions. Evidence that supports our argument regarding 2+ oxidation state for Co ions can also be obtained by the observation of satellite peaks [17–22]. The spectrum that fitted to each satellite peak can be associated with Co^{2+} ions. No additional spectrum corresponding to Co^{3+} ions are observed. This absence or strong suppression of satellite peaks in photoelectron spectrum of Co^{3+} ions, surrounded by an octahedron oxygen environment can be understood as a consequence of electronic structure comprising filled valence level [17, 22]. In Co^{3+} ion, the 3d level splits into low energy triplet t_{2g} and a higher energy doublet e_g level. The lower energy triplet t_{2g} is filled first by all the valence 6 electrons, leading to doublet e_g empty. This corresponds to a low spin state, $S = 0$. Therefore, the charge transfer from ligand to valence orbital is precluded, as a result of it no additional spectrum other than Co^{2+} is found fitted to the satellite peaks. The spin-orbital energy splitting is also another useful way to identify the oxidation state of Co. Experimentally it is confirmed that the divalent and trivalent Co ions possess around 16 and 15 eV spin-orbital splitting respectively [18, 23]. The obtained splitting of 16.1 eV compares favorably with the value of 16 eV of Co^{2+}. Therefore, it can be concluded that Co exists in mixed valence state having a majority of 2+ oxidation state.

The Ta 4f spectrum presented in figure 3(b) can be deconvoluted into 2 doublets; each having two components; $4f_{7/2}$ and $4f_{5/2}$ generated by spin-orbital splitting with separation energy 1.9 eV. The peaks of larger doublet appeared at 25.00 and 26.90 eV correspond to $4f_{7/2}$ and $4f_{5/2}$ components respectively. These values lie just in between doublet of pure Ta metal (21.5 and 23.4 eV) [24] and the doublet of Ta^{5+} (around 26 and 28 eV) [25] ions of Ta_2O_5. This confirms that the Ta ions present on the surface are in oxidized environment with a 4+ oxidation state. Bertaut *et al* [7] have proposed a 5+ oxidation state for Ta ions in $Co_4Ta_2O_9$ ceramics. There are three possibilities for which this reduction in oxidation state of Ta ions present on the surface may take place. The first one is the generation of oxygen vacancies along with a pair of trapped electrons during phase formation at high temperature in the Ta_2O_9 group formed by two adjacent face sharing octahedrons. These trapped electrons reduce the oxidation state of Ta ions from 5+ state to 4+ suboxide state. As a consequence, the TaO_6 octahedral distortion occurs on a large scale. Our early discussion on x-ray diffraction spectra, where TaO_6 octahedron shows larger degrees of polyhedral distortion than the CoO_6 octahedrons, supports this argument. The second possibility is a stabilization process, where Ta –Ta bonding across the face shared TaO_6 octahedra of T_2 dimer takes place by an electrochemical reduction of Ta^{5+} to Ta^{4+}. A similar argument has been put forward by Gupta *et al* [26] in order to explain the oxidation-reduction process in Ta^{5+} ions present in MTa_2O_6 (with M = Co, Fe, Cr, and Ni) ceramics where the octahedral-site edge is shared by two conjugative TaO_6 octahedrons. The third possibility is the partial reduction of Ta^{5+} ions to Ta^{4+} ions in the crystal lattice as a result of the volatilization of Co during the sintering process. Wu *et al* [27] have proposed analogous reasoning for Co containing hexaferrite, $Ba_{0.5}Sr_{1.5}Co_2(Fe_{1-x}Al_x)_{12}O_{22}$ ($x = 0$–0.12) to explain the partial reduction phenomenon of Fe ions from 3+ to 2+ state. Thus, all these possibilities require more attention and investigation in order to explore the chemical properties of this material. However, another small doublet with less intensity at 24.10 and 26.02 eV with separation energy 1.92 eV is a characteristic of Ta suboxide (Ta^{2+}). The presence of large Ta^{4+} doublet suggests that the large area stacks are composed of main ions with 4+ oxidation state (~90%).

The deconvoluted spectra of O 1s spectrum is shown in figure 3(c). The large photo peak centered at 530.89 eV is attributed to the metal-oxygen peak. The spectrum located at the higher energy side of the main peak (532.19 eV) can be assigned to oxygen vacancy. The appearance of a couple of lower energy oxygen spectra at 529.69 and 528.82 eV is possibly a consequence of Co−O tight binding.

Like $Co_4Ta_2O_9$, the x-ray photoelectron spectrum of 2p core level orbital associated with the Co ion present in $Co_4Nb_2O_9$ compound is demonstrated in figure 3(d). The prominent Co $2p_{3/2}$ component can be deconvoluted into two peaks centered at 779.75 and 781.03 eV corresponding to Co^{3+} and Co^{2+} ions respectively, which are in good agreement with previous reports [21, 22]. Similarly, the other spin–orbit component, Co $2p_{1/2}$, is also fitted to two spectra having peak positions at 795.50 and 796.83 eV which can be attributed to Co^{3+} and Co^{2+} respectively. The spin-orbital splitting energy between Co $2p_{3/2}$ and Co $2p_{1/2}$ is ~16.07 eV which reveals that the majority of Co ions do possess 2+ oxidation state. Besides this splitting energy observation, the presence

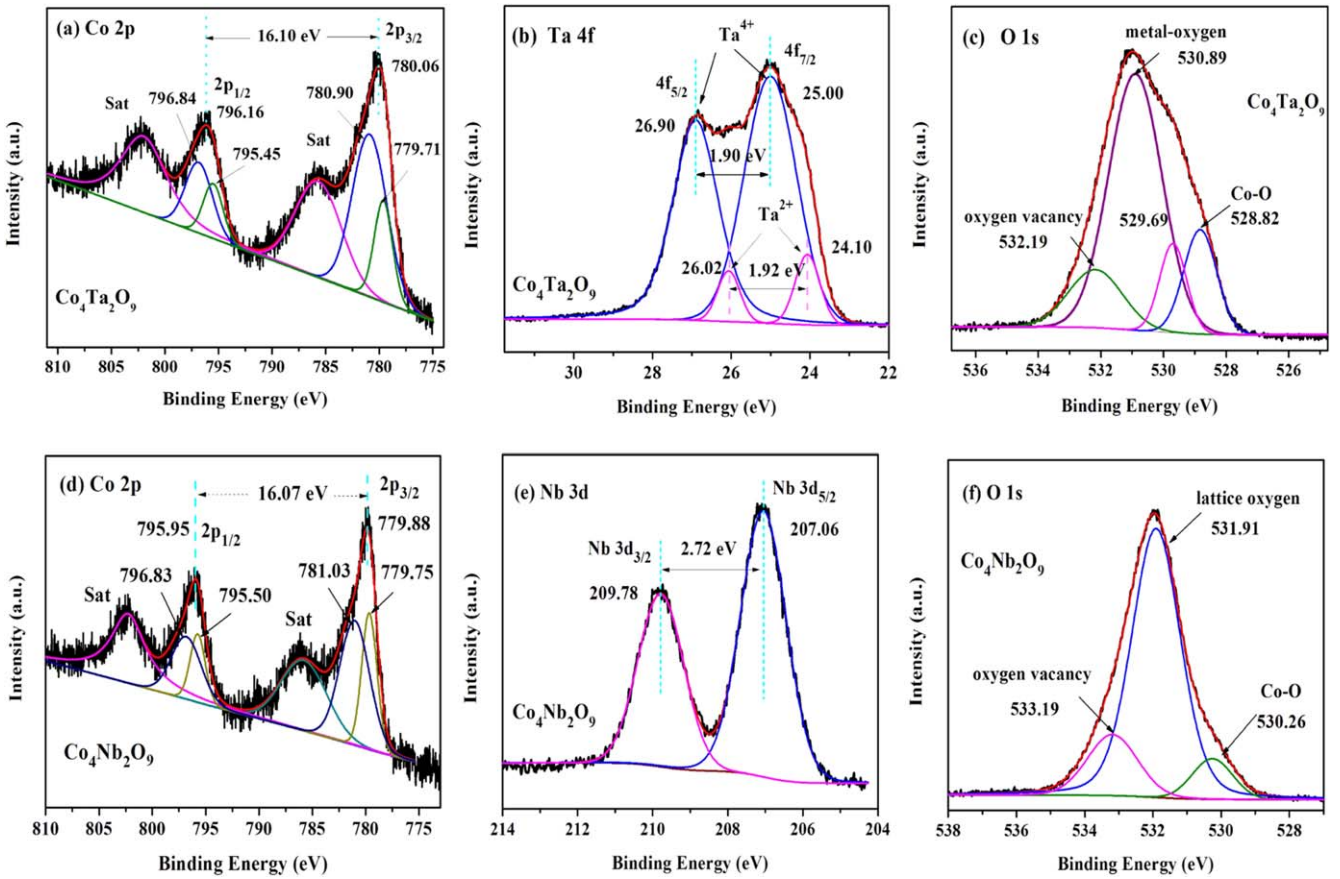

Figure 3. XPS spectra of (a)–(c) Co 2p, Ta 4f and O 1s of $Co_4Ta_2O_9$ and (d)–(f) Co 2P, Nb 3d and O 1s of $Co_4Nb_2O_9$ ceramics.

of Co^{2+} ions in a significant percentage can also be confirmed from a pair of intense shake-up satellite peaks appeared at 786.04 and 802.36 eV.

Figure 3(e) presents the photoelectron spectrum of Nb 3d showing one distinct doublet having components; $3d_{5/2}$ and $3d_{3/2}$. The binding energies for $3d_{5/2}$ and $3d_{3/2}$ are 207.06 and 209.78 eV respectively. This spectrum is deconvoluted to a couple of spectra fitted to each photo-peak suggesting the presence of a single oxidation state for Nb ions. To identify this oxidation state, here a conjectural approach has been used. In this approach, the energy difference between O 1s and Nb $3d_{5/2}$ ($\Delta(O-Nb)$ = BE(O 1s)–BE(Nb $3d_{5/2}$)) has taken into consideration. The energy separation, $\Delta(O-Nb)$ depends on Nb–O bond nature, therefore this method has been preferred to identify the valence state of Nb ions. When Nb–O bond forms, the valence electrons transfer from Nb to O atom procuring the shift of BE to higher energy for Nb $3d_{5/2}$ and to lower energy for O 1s. Atuchin *et al* [15] have also used this technique to establish a relation between Nb–O bond length and binding energy for various oxidation states of Nb ions. They have observed that the maximum value for the separation energy Δ is $\cong$323.50 eV tenable in Nb^{5+}-niobates. However, for Nb^{4+}-niobates like NbO_2 and $Sn_{0.5}NbTiP_3O_{12}$, the separation energy values are 325.03 and 324.30 eV respectively. This shows that Nb^{4+}-niobates exhibit a higher value of Δ than Nb^{5+}-niobates. In our case (from figures 3(e) and (f)), the observed separation energy ($\Delta(O-Nb)$) is 324.85 eV which claims in support of 4+ valence state for Nb ions. This reduction in oxidation state can also be noticed in the same figure where the binding energy corresponding to the photoelectron peaks of Nb 3d of $Co_4Nb_2O_9$ exhibits lower values than the reported [28] values for Nb^{5+} of Nb_2O_5 ($\sim$207.5 and 210.1 eV for Nb $3d_{5/2}$ and Nb $3d_{3/2}$ photo-peak respectively). Darlinski and Halbritter [29] have revealed that a reduction in oxidation state of Nb ions takes place in Nb_2O_5, because of the stoichiometry compensation process. To compensate stoichiometry in NbO_6 octahedron that presents in Nb_2O_5, an oxygen vacancy V_o is introduced by the generation of defect complex $Nb^{4+}V_oNb^{4+}$ during the electron transfer process from central Nb atom to corner O atoms. The resultant defect complex $Nb^{4+}V_oNb^{4+}$ localizes electrons which later participate as charge carriers in conduction process. Therefore, in $Co_4Nb_2O_9$ ceramics, the Nb_2O_9 groups need stoichiometric compensation. As a result, reduction in the oxidation state of Nb ions takes place along with the generation of oxygen vacancy. The contributions of these vacancies to conduction and relaxation processes are discussed briefly in our next segments.

The XPS spectrum of O 1s core level of $Co_4Nb_2O_9$ ceramic is demonstrated in figure 3(f). Out of three fitting peaks, the main photo peak that appears at 531.91 eV can be assigned to O^{2-} ions of metal-oxygen bonding whereas the peak appears at higher energy (533.19 eV) can be referred to either oxide ion vacancy or hydroxyl oxygen (O−H) group [30, 31] present on the surface. The lower energy oxygen

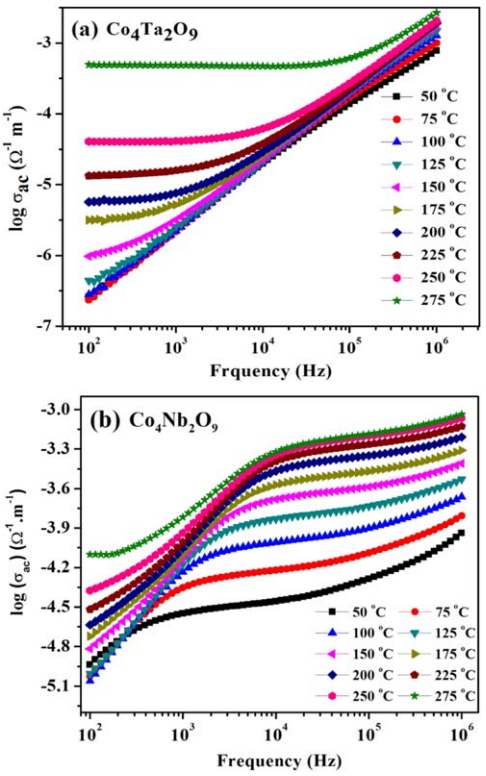

Figure 4. Conductivity spectra of (a) $Co_4Ta_2O_9$ and (b) $Co_4Nb_2O_9$ ceramics.

spectrum appeared at 530.26 eV is possibly an outcome of tight binding Co−O bond.

3.3. Conductivity

To study the electrical properties for the electronic applications of these materials, the frequency-dependent ac conductivity (σ_{ac}) of $Co_4Ta_2O_9$ and $Co_4Nb_2O_9$ ceramics was carried out in the radio wave frequency range of 100 Hz–1 MHz. The spectra obtained at different temperatures are shown in figure 4. For $Co_4Ta_2O_9$, the dispersion of σ_{ac} with frequency is composed of two regions (figure 4(a)); the frequency-independent plateau in lower frequency region and the frequency dependent sharp increase in the upper frequency region. As the frequency increases, the hopping of carriers also increase [32], resulting in an increase in ac conductivity. At higher frequency range (in figure 4(a)), all the curves seem to be merged irrespective of their temperature, which is a common phenomenon in a conventional disordered system, suggesting the existence of common relaxation process [33, 34]. Thus, an additional term, $B\omega^m$ ($m \sim 1$) is required in Jonscher's power law [35–37] as a near-constant loss. With rising in temperature, curves exhibit frequency-independent flat region showing the dominance of dc conduction. For $Co_4Nb_2O_9$, three regions appear in ac conductivity curves (in figure 4(b)); a polarization region, a frequency-independent plateau region, and a strong frequency dependent dispersive region. The intermediate plateau region can be explained by the hopping model where carriers hop from one site to the neighboring vacancy site contributing to dc conduction σ_{dc}. The deviation observed in σ_{dc} at lower frequency refers to space charge polarization at blocking electrodes. On the other hand, the dispersion nature of σ_{ac} at higher frequency deals with the alternate hopping of carriers along with their relaxation process [12, 38]. In this case, no additional term is required in the power-law expression because of the dispersive nature of conductivity curves at the high-frequency region.

The relationship between conductivity (σ) and frequency can be expressed by the Jonscher's power law i.e.:

$$\sigma_{ac}(T) = \sigma_{dc} + A(T)\omega^{\eta}(T) + B\omega^{m}, \tag{2}$$

where A and B are constants, ω is the angular frequency and the exponent η and m are dimensionless. The temperature-dependent constant A is related to the carrier hopping frequency, ω_p by the relation [39], $A = K(\omega_p)^{1-n}$. The hopping increases with rising in temperature and so as conductivity. Thus, the constants A and K behave as temperature-dependent entities. The values of exponent η have been obtained by fitting equation (2) into the $\log(\sigma_{ac})$ versus $\log(\omega)$ curve. The variation of η with temperature is shown in figure 5(a) which depicts the types of mechanism that takes place in conduction process. Generally, there are three mechanisms for conduction process [40–43]; the first one is quantum mechanical tunneling, where η is temperature independent, the second is small polaron tunneling, where η increases with temperature and the third one is correlated barrier hopping (CBH), where η behaves inversely with temperature. Apart from these three mechanisms, there is also a possibility of overlapping large polaron tunneling (OLPT), where η increases with temperature after achieving a minimum value [44]. In the case of $Co_4Ta_2O_9$ (in figure 5(a)), both small polaron conduction and CBH mechanisms are found to be probable in different temperature regimes. In low-temperature region (up to 200 °C), the η value increases gradually with rising in temperature, which indicates the possibility of small polaron tunneling, whereas for the high-temperature region (above 200 °C), η decreases rapidly suggesting in favor of correlated barrier-hopping. However, for $Co_4Nb_2O_9$, η decreases gradually till the temperature approaches 250 °C and beyond this temperature it starts increasing. It depicts that OLPT mechanism is predominant in the transport process.

In order to investigate the conduction mechanisms in various temperature regimes at different frequencies, the values of activation energy (E_a) for electrical conduction were estimated using Arrhenius relation

$$\sigma_{ac} = \sigma_0 \exp\left(-\frac{E_a}{k_B T}\right), \tag{3}$$

where E_a represents activation energy, σ_0 stands for pre-exponential factor and k_B for Boltzmann constant. Figures 5(b) and (c) exhibit logarithm of conductivity ($\log(\sigma_{ac})$) versus the inverse of temperature ($1000/T$) at different frequencies for $Co_4Ta_2O_9$ and $Co_4Nb_2O_9$ compositions respectively. In these figures, the ac conductivity increases with temperature and exhibits two regions of different conduction processes. The conductivity in the region I strongly depends on the temperature whereas in region II, it is weakly dependent. The

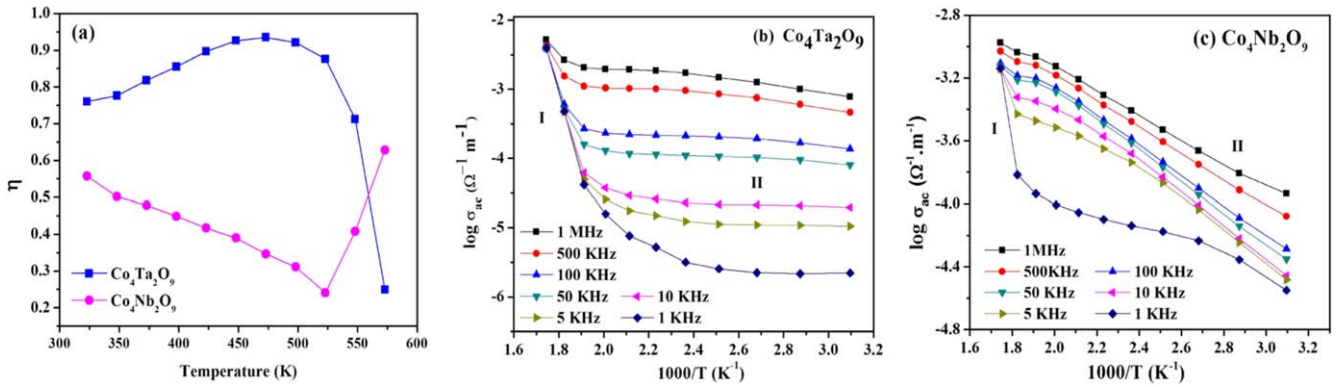

Figure 5. (a) Variation of η with temperature; ac conductivity versus 1000/T (K^{-1}) plot of (b) $Co_4Ta_2O_9$ and (c) $Co_4Nb_2O_9$ ceramics.

Table 4. Activation energy (eV) for the $Co_4Ta_2O_9$ and $Co_4Nb_2O_9$ ceramics at different temperature regime.

	$Co_4Ta_2O_9$		$Co_4Nb_2O_9$	
Frequency (kHz)	I	II	I	II
1	0.747	0.017	0.408	0.065
5	0.718	0.017	0.181	0.088
10	0.706	0.013	—	0.079
50	0.661	0.013	—	0.079
100	0.491	0.022	—	0.076
500	0.308	0.034	—	0.068
1000	0.227	0.035	—	0.063

conduction activation energy E_a for both the regions at different frequencies has been calculated using Arrhenius relation and is presented in table 4.

In the conduction process of corundum type materials, the possible mobile charge carriers are electrons, holes and oxygen vacancies [12]. The formation of oxygen vacancies leads to the creation of conduction electrons which later take part in oxidation reduction process. This process can be described by the Kroger–Vink notation;

$$O_o^x \rightarrow \frac{1}{2}O_2(g) + V_O^{\bullet\bullet} + 2e, \tag{4}$$

where $V_O^{\bullet\bullet}$ represents the oxygen vacancy with two excess positive charges and O_o^x represents neutral lattice oxygen. The oxygen vacancy associated $(Ta/Nb)_2O_9$ group traps these generated electrons and reduces the oxidation state of Ta/Nb ions from 5+ to 4+

$$2(Ta/Nb)^{5+} + 2e \leftrightarrow 2(Ta/Nb)^{4+}. \tag{5}$$

After thermal activation, both the oxygen vacancy and trapped electrons actively participate in the conduction process. Generally, these carriers need high activation energy for conduction. In table 4, the activation energies corresponding to the region I (the high-temperature region) exhibit large values as compared to region II (the low-temperature region). For region I, at 1 kHz frequency the activation energy is ~0.747 eV, whereas at 1 MHz it decreases to ~0.227 eV in $Co_4Ta_2O_9$ ceramic. This long-range of variation in the activation energy for a specific temperature regime indicates that the hopping of carriers is from long-range to short-range and the mobile charge carriers are mostly the vacancy trapped electrons. In the CBH process [44], these vacancy trapped electrons associated with Ta_2O_9 group hop between neighboring site pairs of separation distance R over a potential barrier W

$$W = W_m - (e^2/(\pi\varepsilon\varepsilon_0 R)), \tag{6}$$

where W_m is the trap depth, ε is the dielectric constant and ε_0 is the permittivity of free space. The second term of the equation is associated with the barrier lowering, generated due to the overlapping of traps. At low field and high temperature, the conductivity spectra are dominated by the dc conduction and the electrons follow the shortest hopping distance, R_{min} as their favorable path for charge transport. The oxygen vacancies are mostly associated with Ta_2O_9 groups. Therefore, the distance covered by an electron to hop between two defect/trap sites is comparable to the separation distance between groups. This separation distance R varies from pairs to pairs, so does W_m. Along a and b axes, the group separation is ~3.010 Å whereas, along c-axis, it is ~3.853 Å. From equation (6), taking the conduction activation energy $W =$ 0.747 eV and the intergroup separation $R_{min} = 3.01$ Å, one can get the trap depth for oxygen vacancy $W_m =$ 1.208 eV.

In table 4, region II exhibits smaller values of the conduction activation energy for $Co_4Ta_2O_9$ composition. The presence of mixed oxidation states for Co ions may lead to the transfer of charge between $Co^{2+} \leftrightarrow Co^{3+}$. This exchange interaction via hopping generates electric dipole, which leads to a polaronic process. On the contrary, in the case of small polaron, the deformation around two sites does not overlap with each other and the activation energy is independent of their separation distance. In this case, the deformation energy is confined to the local bonding changes. Usually, polaron is composed of an electron along with lattice distortion. In case of small polaron conduction, the hopping is short-range, i.e. the hopping distance is less than crystal parameters. Similarly, for $Co_4Nb_2O_9$, two regions of different conduction processes are observed up to 5 kHz frequency, where the space charge electrode polarization plays a significant role. Beyond this frequency, a single conduction process is observed for the entire temperature regime, where the OLPT model stands well. Long [44] has proposed that in the OLPT model, the polaron

Table 5. The parameters of best fitted to the experimental data of total ac conductivity by OLPT model for $Co_4Nb_2O_9$ ceramics.

Parameters	Fitted values
r_P (Å)	24.49
α (Å^{-1})	1.065
$N(E_f)$ ($\times 10^{21}$ eV^{-1} cm^{-3})	13.20
W_{HO} (eV)	0.099

energy can be derived from the polarization changes in the deformed lattice. When a polaron-well extends over several atomic distances, due to the long-range of Coulomb interaction in the lattice, an overlapping of potential well of the degenerate site is obvious. As a consequence the activation energy decreases. The corresponding resultant excitation is called large polaron or dielectric polaron. An expression for ac conductivity and frequency exponent for OLPT model [41, 44] is given by

$$\sigma(\omega) = \left[\frac{\pi^4 e^2 k_B^2 T^2 \{N(E_f)\}^2}{12}\right] \times \frac{\omega R_\omega^4}{2\alpha k_B T + \frac{w_{HO} r_p}{R_\omega^2}}, \quad (7)$$

$$\eta = 1 - \frac{8\alpha R_\omega + \frac{6W_{HO} r_P}{R_\omega k_B T}}{\left[2\alpha R_\omega + \frac{W_{HO} r_P}{R_\omega k_B T}\right]^2}, \quad (8)$$

where α is the inverse localization length, R_ω is the hopping length at frequency ω, r_P is the polaron radius, $N(E_f)$ is the density of states at Fermi level and W_{HO} is the activation energy associated with the charge transfer between the overlapping sites. Equation (7) exhibits good agreement with the experimental data when it is fitted with ac conductivity versus frequency spectra. The parameters, $N(E_f)$, W_{HO}, r_P and α obtained by fitting are listed in table 5. The obtained value of W_{HO} (0.099 eV) is close to the conduction activation energy E_a (0.088 eV) and the polaron radius r_P (24.49 Å) is of the several crystal orders. This supports our argument of large polaron conduction.

3.4. Relaxation process study

Electric modulus formalism is utilized to explain the charge transport processes like; electrical transport, ion dynamics and conductivity relaxation phenomena due to its ability to suppress the electrode polarization at low frequencies [45, 46]. It is also an important and convenient tool to study the free charge relaxation mechanism, which is not clearly detected in dielectric permittivity. Complex electric modulus is the reciprocal of complex permittivity, $M^*(\omega) = 1/\varepsilon^*$. It can be expressed as

$$M^*(\omega) = \frac{1}{\varepsilon^*(\omega)} = M' + iM'' = M_\infty\left[1 - \int_0^\infty \left(-\frac{d\Phi(t)}{dt}\right)\exp(-i\omega t)dt\right], \quad (9)$$

where $M_\infty = 1/\varepsilon_\infty$, with ε_∞ being the high-frequency limit of the real part of permittivity, and the function $\phi(t)$ is the time evolution of the electric field within the materials [47].

For $Co_4Ta_2O_9$ ceramic, the variation of the imaginary part of electric modulus M'' as a function of frequency at different temperatures are presented in figure 6(a). In this figure, the relaxation peak shifts towards higher frequency region with increase in temperature which reveals that relaxation is a thermally activated process. With the rise in temperature the movement of charge carriers becomes faster, resulting in less relaxation time [43]. Therefore, shifting of peak position, towards higher frequency range is observed. Each relaxation peak represents a transition from long-range to the short-range motion of charge carriers with the increase in frequency. In the low-frequency side of M'' peak, the charge carriers are able to move long distances, i.e. hopping from one site to the neighboring site, whereas in the high-frequency side of the peak the charge carriers are confined to their potential wells resulting in a localized motion [48, 49]. This localized motion leads to behaving as a polarized corporate entity. The asymmetry in peak broadening reveals that the relaxation is of non-Debye type, because of the presence of various relaxation time constants [50]. Crystal distortion plays a major role in the relaxation process. As a consequence of octahedral distortion, interionic distances corresponding to Co−O in CoO_6 and Ta−O in TaO_6 polyhedra vary in between 2.0–2.3 Å and 1.7–2.3 Å respectively (in table 2). Angles between the central cation with its corner anions in an octahedron exhibit a significant deviation from its ideal values, 90° and 180°. Because of such distortion, various potential minima are generated within the octahedron. As a consequence, the central cation hops among these potential minima with different strengths resulting out broad relaxation time distributions. It is noticeable that all relaxation peaks start appearing beyond 150 °C within the frequency range of interest. This suggests that above 150 °C (the high-temperature region), carriers (oxygen vacancies and trapped electrons) obtain sufficient energies to overcome the potential barriers by a long-range hopping process.

The most probable conductivity relaxation time τ_c corresponds to the average residence time which can be derived by substituting the peak frequency f_{max} of M'' in the relation $2\pi f_{max}\tau_c = 1$. Figure 6(b) shows the logarithmic plot of relaxation times with the reciprocal of absolute temperature for $Co_4Ta_2O_9$ ceramics. It is observed that this plot follows closely the Arrhenius equation

$$\tau = \tau_0 \exp(E_m/k_B T), \quad (10)$$

where τ_0 refers to the relaxation time at infinite temperature and E_m refers to the migration energy of charge carrier for the hopping process. The migration energy E_m is found to be 0.754 eV for $Co_4Ta_2O_9$ ceramic which is close to the conduction activation energy E_a (0.747 eV) obtained for region I. The small variation in the second decimal point can be explained using Rolling's observation [51]. It indicates that the 'window effect' is generated when a specific frequency regime corresponding to the M'' peak is emphasized more than other frequency regimes. This selective approach restricts us to select the values of relaxation time associated with different regimes. Therefore, a small discrepancy is

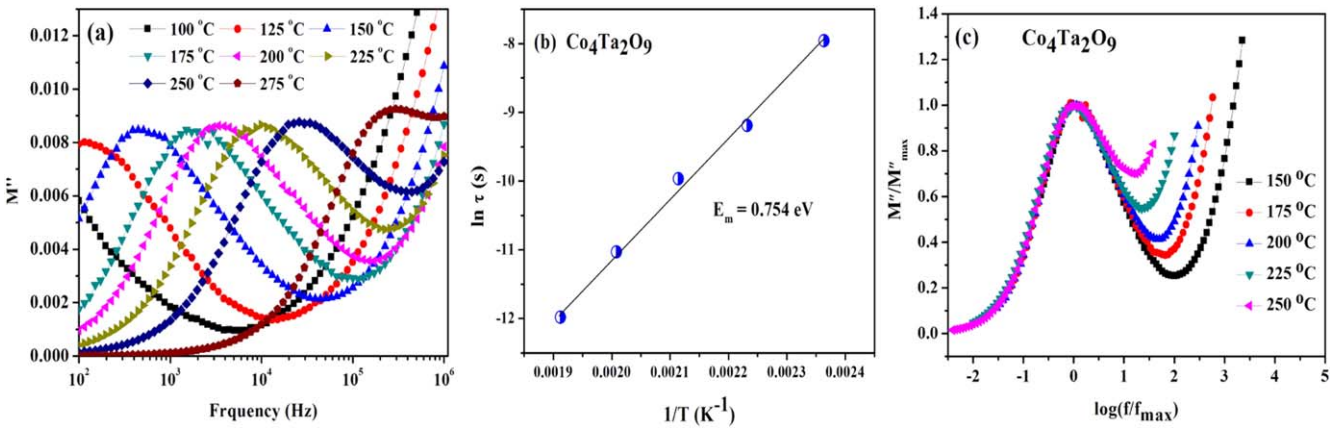

Figure 6. (a) Electric modulus (M'') as a function of frequency, (b) Arrhenius plots of relaxation time (τ) with inverse of temperature, (c) modulus master curves at various temperature for $Co_4Ta_2O_9$ ceramic.

observed between conduction activation energy (E_a) and migration energy (E_m) values.

However, the scaling behavior of the modulus spectra has been used for further analysis of relaxation dynamics. For $Co_4Ta_2O_9$ ceramic, the variation of normalized the imaginary part of electric modulus (M''/M''_{max}) with normalized frequency ($\log(f/f_{max})$) at different temperatures are shown in figure 6(c). Due to the shifting of relaxation peaks out of the frequency window, few modulus spectra obtained below 150 °C and above 250 °C could not be included in the master curve plot. The overlapping of modulus curves corresponding to different temperatures into a single master curve, except on the high-frequency tail, indicates that the dynamic process occurs at different time scales and possesses the same activation energy [52]. The obtained full width half maxima (FWHM) value of the master modulus curve is 1.852 decades which is wider than the typical Debye peak width (1.142 decades) [53]. This explains that the relaxation mechanism is of non-Debye in nature.

The normalized modulus curves can also be expressed in terms of the exponential decay function [54]

$$\phi(t) = \exp(-t/\tau)^{\beta}, (0 < \beta < 1), \tag{11}$$

where $\phi(t)$ is an electrical relaxation function or Kohlrausch–Williams–Watts function and β is the Kohlrausch exponent parameter. The value of β can be evaluated using the width (FWHM) of master modulus curve in the following relation established by Dixon [53]

$$\beta = 1 - 1.047\left(1 - \frac{1.142}{\text{FWHM}}\right). \tag{12}$$

For the Debye type relaxation process, the β value must be equal to unity. The smaller this value the larger is the deviation in ideal Debye relaxation. In our case, the obtained β value for $Co_4Ta_2O_9$ ceramic is 0.598 which gives a clear indication of the non-Debye nature of relaxation. β is also useful in order to analyze the ionic concentration present in a system where the concentration of mobile ions varies [51]. The β value increases with a decrease in ionic concentration and it approaches unity (for Debye type relaxation) when the concentration is low.

However, for $Co_4Nb_2O_9$ ceramic, no prominent relaxation peak is observed in the imaginary part of the electric modulus curve within the frequency range of 100 Hz–1 MHz (figure 7(a)). It is known that the electric modulus is the reciprocal of complex permittivity. The imaginary part of permittivity ε'' which deals with the dielectric loss factor includes dipolar loss and conduction loss [55]. Due to the dominance of the space charge polarization process in the lower-frequency region, the dipolar relaxation/rotation can be visualized in the high-frequency range (above 5 kHz) in the dielectric loss spectra. The ratio between the real and imaginary part of permittivity is called dielectric loss factor. Figure 7(b) shows the variation of dielectric loss tangent ($\tan\delta$) with frequency for $Co_4Nb_2O_9$ sample at various temperatures. Each spectrum exhibits a single dielectric loss peak appeared due to dipolar polarization. Like ferrite samples [27], electron exchanges take place between Co^{2+} and Co^{3+} states. These electrons induce polarization around Co ions to form polarons. This electron transfer is a thermally activated process. Therefore, loss tangent peak shifts towards higher frequency with the rise in temperature suggesting a gradual reduction in relaxation time. The peak frequency exhibits Arrhenius-type behavior

$$f_{\tan\delta} = f_0 \exp(-E_d/k_B T), \tag{13}$$

where f_0 is the pre-exponential factor and E_d is the activation energy for dipolar relaxation or rotation. Figure 7(c) shows the dielectric loss peak frequency ($f_{\tan\delta}$) versus the inverse of temperature for $Co_4Nb_2O_9$ ceramic. The activation energy obtained from the slope of the dielectric relaxation line is found to be 0.093 eV, which is close to the conduction activation energy of 0.088 eV derived for 5 kHz frequency (in table 4) and to the activation energy W_{HO} associated with charge transfer between overlapping sites of 0.099 eV (in table 5), suggesting in favor of OLPT model. This conduction of large polarons among the equivalent lattice sites in the presence of applied electric field leads to the reorientation of

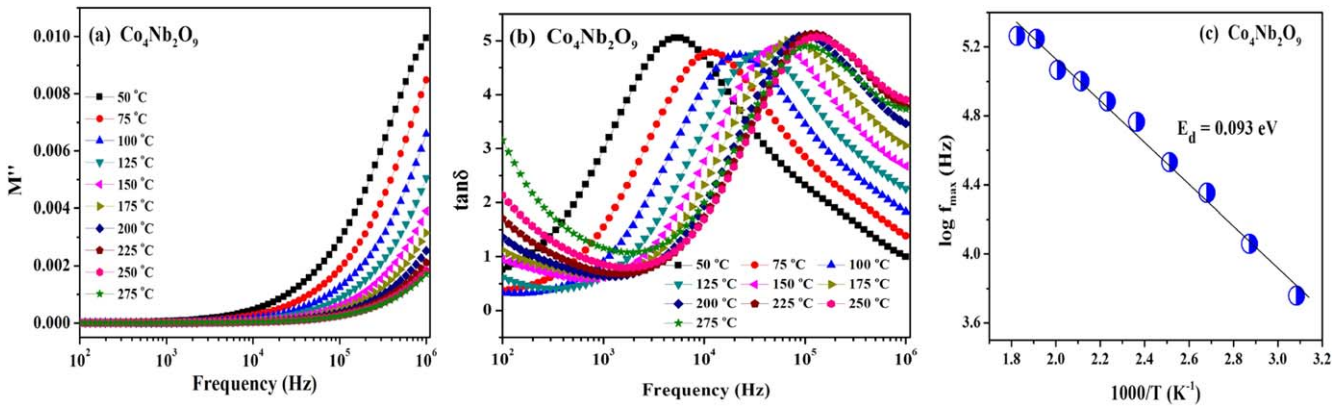

Figure 7. (a) Electric modulus (M'') as a function of frequency, (b) frequency spectra of dielectric loss tangent (tan δ) at various temperatures, (c) Arrhenius plots of dielectric loss peak frequency of $Co_4Nb_2O_9$ ceramic.

electric dipole [56, 57], which provides the frequency-dependent nature of complex dielectric permittivity.

In this article, it can be visualized that the crystal distortion and the elemental oxidation states play a significant role in conduction and relaxation processes. Apart from the conduction and relaxation mechanisms, the electrical properties of materials can also be explored more by other various studies like; impedance study, grain–grain boundary contribution study and dielectric study etc. As the sampling depth (3λ) for XPS is ~3–10 nm, therefore the surface chemistry may differ from internal elemental characteristics. Thus, a depth profile study of the oxidation state using XPS can provide more information about the nature of ionic states. Therefore, these corundum type ceramics need more attention to improve the understanding of their properties.

4. Conclusions

In this article, the structural, elemental and electrical conduction properties have been studied extensively for corundum-type $Co_4Ta_2O_9$ and $Co_4Nb_2O_9$ ceramics. The refined x-ray diffraction results confirm the formation of single-phase for $Co_4Ta_2O_9$, whereas for $Co_4Nb_2O_9$, an additional phase having less weight percentage of $CoNb_2O_6$ coexists with the primary phase. The obtained crystal structures exhibit that the unit cells of both the compositions are isostructural to $Mg_4Ta_2O_9$. The calculation of the relative degree of polyhedral distortion reveals that $(Ta/Nb)O_6$ octahedrons are more distorted than CoO_6 octahedrons. Despite these polyhedral distortions, no structural phase transition is observed in temperature-dependent x-ray diffraction spectra. The x-ray photoelectron spectrum of core level electrons depicts that the majority of Co ions exist in 2+ oxidation state whereas, Ta and Nb ions exhibit a reduction in their oxidation state from 5+ to 4 + , which is an outcome of the generation of oxygen vacancies along with trapped electrons. The O 1s spectra support the oxygen vacancy argument which has been confirmed later by charge transport study in conduction analysis section.

The effects of oxidation-reduction and the defect chemistry on conduction and relaxation processes have been investigated for these compositions. In $Co_4Ta_2O_9$ ceramics, two regions of different conduction processes have been identified in the logarithm of conductivity versus inverse temperature plot. At high-temperature region, the CBH process is the dominating conduction mechanism, where oxygen vacancies along with their trapped electrons are the major charge carriers. However, in the low-temperature region, small polarons, generated by the exchange interaction between Co^{2+} and Co^{3+} ions play a significant role in conduction process. In $Co_4Nb_2O_9$ ceramic, single conduction process is observed beyond 5 kHz frequency, where the OLPT model fits well with the conductivity versus frequency plot and below this frequency electrode polarization prevails. The fitted results reveal that polaronic radius and the polaron energy for tunneling are 24.49 Å and 0.099 eV respectively. In complex electric modulus analysis of $Co_4Ta_2O_9$ ceramic, the obtained migration energy E_m of 0.754 eV is almost close to the conduction activation energy E_a of 0.747 eV, suggesting identical carriers are participating in both conduction and relaxation processes. Similarly, in the case of $Co_4Nb_2O_9$ ceramic, the dipolar relaxation energy E_d of 0.093 eV is found close to both conduction activation energy E_a of 0.088 eV derived for 5 kHz frequency and large polaron conduction energy W_{HO} of 0.099 eV obtained by fitting the OLPT model. The non-Debye nature of broad relaxation peaks appeared in the frequency window can be ascribed to the existence of several potential minima for the charge carriers within the distorted octahedra.

Acknowledgments

The author, Mr P Mohanty acknowledges the CSIR, India for providing financial assistance (09/554(0044)/2018-EMR-I). The authors are thankful to ACMS, IIT Kanpur for availing XPS and CIF, BIT Mesra, India for conducting various experiments.

ORCID iDs

Parthasarathi Mohanty https://orcid.org/0000-0002-1564-7064

References

[1] Huang C–L, Yang W-R and Chen Y-R 2010 *J. Alloys Compd.* **495** L5–7
[2] Keshri S, Mohanty P and Gupta V R 2017 *J. Mater. Sci. Mater. Electron.* **28** 14436–45
[3] Solovyev I V and Kolodiazhnyi T V 2016 *Phys. Rev.* B **94** 094427
[4] Fang Y, Song Y Q, Zhou W P, Zhao R, Tang R J, Yang H, Lv L Y, Yang S G, Wang D H and Du Y W 2014 *Sci. Rep.* **4** 3860
[5] Fang Y, Yan S, Zhang L, Han Z, Qian B, Wang D and Du Y 2015 *J. Am. Ceram. Soc.* **98** 2005–7
[6] Khanh N D, Abe N, Sagayama H, Nakao A, Hanashima T, Kiyanagi R, Tokunaga Y and Arima T 2016 *Phys. Rev.* B **93** 075117
[7] Bertaut E F, Corliss L, Forrat F, Aleonard R and Pauthenet R 1961 *J. Phys. Chem. Solids* **21** 234–51
[8] Fischer E, Gorodetsky G and Hornreich R M 1972 *Solid State Commun.* **10** 1127–32
[9] Kan A, Ogawa H, Yokoi A and Nakamura Y 2007 *J. Eur. Ceram. Soc.* **27** 2977
[10] Tarakina N V, Tyutyunnik A P, Zubkov V G, D'yachkova T V, Zainulin Y G, Hannerz H and Svensson G 2003 *Solid State Sci.* **5** 459–63
[11] Castellanos R M A, Bernès S and Vega-González M 2006 *Acta Cryst.* E **62** i117–9
[12] Mohanty P 2016 *RSC Adv.* **6** 73748–59
[13] Kolodiazhnyi T, Sakurai H and Vittayakorn N 2011 *Appl. Phys. Lett.* **99** 132906
[14] Kolodiazhnyi T, Belik A A, Ozawa T C and T-Muromachi E 2009 *J. Mater. Chem.* **19** 8212–5
[15] Atuchin V V, Kalabin I E, Kesler V G and Pervukhina N V 2005 *J. Electron Spectrosc. Relat. Phenom.* **142** 129
[16] Hofmann S 2013 *Auger- and X-Ray Photoelectron Spectroscopy in Materials Science* (Berlin: Springer)
[17] Daheron L, Martinez H, Dedryvere R, Baraille I, Menetrier M, Denage C, Delmas C and Gonbeau D 2009 *J. Phys. Chem.* C **113** 5843–52
[18] Okamoto Y, Nakano H, Imanaka T and Teranishi S 1975 *Bull. Chem. Soc. Japan* **48** 1163–8
[19] Frost D C, McDowell C A and Woolsey I S 1974 *Mol. Phys.* **27** 1473–89
[20] Mclntyre N S and Cook M G 1975 *Anal. Chem.* **47** 2208–13
[21] Tan B J, Klabunde K J and Sherwood P M A 1991 *J. Am. Chem. Soc.* **113** 855–61
[22] Vaz C A F, Prabhakaran D, Altman E I and Henrich V E 2009 *Phys. Rev.* B **80** 155457
[23] Ivanova T, Naumkin A, Sidorov A, Eremenko I and Kiskin M 2007 *J. Electron Spectrosc. Relat. Phenom.* **156-158** 200–3
[24] Simpson R, White R G, Watts J F and Baker M A 2017 *Appl. Surf. Sc.* **405** 79–87
[25] Goncalves R V, Wojcieszak R, Uberman P M, Teixeira S R and Rossi L M 2014 *Phys. Chem. Chem. Phys.* **16** 5755–62
[26] Gupta A, Singh P, Celio H, Mullins C B and Goodenough J B 2015 *Inorg. Chem.* **54** 2009–16
[27] Wu M X, Zhong W J, Gao X S, Liu L J and Liu Z W 2014 *J. Appl. Phys.* **116** 224103
[28] Coskun O D, Demirel S and Atak G 2015 *J. Alloy. Comp.* **648** 994–1004
[29] Darlinski A and Halbritter J 1987 *Surf. Interface Anal.* **10** 223–37
[30] Deng Q, Li M, Wang J, Zhang P, Jiang K, Zhang J, Hu Z and Chu J 2017 *Sci. Rep.* **7** 1883
[31] Hota M K, Bera M K and Maiti C K 2012 *Semicond. Sci. Technol.* **27** 105001
[32] Sebastian R M, Xavier S and Mohammed E M 2015 *Ferroelectrics* **481** 48–56
[33] Sidebottom D L 2009 *Rev. Mod. Phys.* **81** 999–1014
[34] Karahaliou P K, Xanthopoulos N, Krontiras C A and Georga S N 2012 *Phys. Scr.* **86** 065703
[35] Sakellis I 2011 *Appl. Phys. Lett.* **98** 072904
[36] Jonscher A K 1977 *Nature* **267** 673
[37] Jonscher A K 1983 *Dielectric Relaxation in Solids* (London: Chelsea Dielectric Press)
[38] Narayanan S, Baral A K and Thangadurai V 2016 *Phys. Chem. Chem. Phys.* **18** 15418–26
[39] Fanggao C, Saunders G A, Wei Z, Almond D P, Cutroni M and Mandanici A 1998 *Solid State Ion.* **109** 89–100
[40] Elliot S R 1987 *Adv. Phys.* **36** 135–217
[41] Ghosh A 1990 *Phys. Rev.* B **42** 1388
[42] Gopalan E V, Malini K A, Saravanan S, Kumar D S, Yoshida Y and Anantharaman M R 2008 *J. Phys. D: Appl. Phys.* **41** 185005
[43] Pandit P, Satapathy S and Gupta P K 2011 *Physica* B **406** 2669–77
[44] Long A R 1982 *Adv. Phys.* **31** 553–637
[45] Dam T, Jena S S and Pradhan D K 2016 *Phys. Chem. Chem. Phys.* **18** 19955–65
[46] Mahato D K and Sinha T P 2015 *J. Alloy. Comp.* **634** 246
[47] Liu J, Duan C-G, Yin W-G, Mei W N, Smith R W and Hardy J R 2003 *J. Chem. Phys.* **119** 2812–9
[48] Dissado L A and Hill R M 1984 *J. Chem. Soc., Faraday Trans. 2* **80** 291–319
[49] Hill R M and Dissado L A 1982 *J. Phys. C: Solid State Phys.* **15** 5171
[50] Tiwari B and Choudhary R N P 2010 *J. Alloy. Comp.* **493** 1–10
[51] Roling B 1998 *Solid State Ion.* **105** 185–93
[52] Ramakumar S, Satyanarayana L, Manorama S V and Murugan R 2013 *Phys. Chem. Chem. Phys.* **15** 11327–38
[53] Dixon P K 1990 *Phys. Rev.* B **42** 8179–86
[54] Chowdari B V R and Gopalakrishnan R 1987 *Solid State Ion.* **23** 225–33
[55] Baral A K, Narayanan S, Ramezanipour F and Thangadurai V 2014 *Phys. Chem. Chem. Phys.* **16** 11356–65
[56] Maity S K, Dutta A, Kumar S and Sinha T P 2013 *Phys. Scr.* **88** 065702
[57] Ang C, Yu Z, Jing Z, Lunkenheimer P and Loidl A 2000 *Phys. Rev.* B **61** 3922–6